Supporting Information for "Glacial cycle ice-sheet evolution controlled by ocean bed properties "

C. Schannwell[1], R. Drews[1], T.A. Ehlers[1], O.Eisen[2,3], C. Mayer[4], M. Malinen[5], E.C. Smith[2], and H. Eisermann[2]

[1]Department of Geosciences, University of Tübingen, Tübingen, Germany

[2]Glaciology, Alfred Wegener Institute, Helmholtz Centre for Polar and Marine Research, Bremerhaven, Germany

[3]Department of Geosciences, University of Bremen, Bremen, Germany

[4]Bavarian Academy for Sciences and Humanities, MunichCSC-IT Center for Science Ltd., Espoo, Finland, Germany

[5]CSC-IT Center for Science Ltd., Espoo, Finland

1. Stable groundging-line positions

In total there are four distinct periods in which the grounding line exhibits stability over several thousand years. Because the hard bed simulation shows larger magnitudes of grounding-line migration, we will focus on this simulation. However, while the position of the stable grounding-line differs between hard bed and soft bed simulations, the relative timing of the periods of stability are very similar, hinting that these stable configurations might be to first order controlled by a common model forcing (e.g. sea level) or boundary condition (e.g. bathymetry). Three out of modelled four stable grounding-line positions occur in the advance phase (0-20,000 years) and one occurs in the retreat phase (20,000-

40,000 years, Figure S1). However, the third stable grounding-line position is present in both periods with this particular configuration being stable for 8,000 years in the hard bed simulation (2,000 years before LGM - 6,000 years after LGM). While the specific timing of the stable grounding-line periods might not be correct due to the employed modelling approach, these modelled positions can still serve as spatial markers of areas where depositional landforms such as Grounding-Zone Wedges (GZWs) may be found.

2. Model description

2.1. Ice flow equations

Ice flow is dominated by viscous forces which permits the dropping of the inertia and acceleration terms in the linear momentum equations. The Elmer/Ice ice-sheet model (Gagliardini et al., 2013) solves the complete 3D equation for ice deformation. This results in the Stokes equations described by

$$div\boldsymbol{\sigma} = -\rho_i \boldsymbol{g}. \tag{1}$$

Here, $\boldsymbol{\sigma} = \boldsymbol{\tau} - p\boldsymbol{I}$ is the Cauchy stress tensor, $\boldsymbol{\tau}$ is the deviatoric stress tensor, $p = -tr(\boldsymbol{\sigma})/3$ is the isotropic pressure, $\boldsymbol{I}$ the identity tensor, ρ_i the ice density, and $\boldsymbol{g}$ is the gravitational vector. Ice flow is assumed to be incompressible which simplifies mass conservation to

$$div\boldsymbol{u} = 0, \tag{2}$$

with $\boldsymbol{u}$ being the ice velocity vector. Here we model ice as an isotropic material. Its rheology is given by Glens flow law which relates the deviatoric stress $\boldsymbol{\tau}$ with the strain rate $\dot{\boldsymbol{\epsilon}}$:

$$\boldsymbol{\tau} = 2\eta\dot{\boldsymbol{\epsilon}}, \tag{3}$$

where the effective viscosity η can be expressed as

$$\eta = \frac{1}{2} E B \dot{\boldsymbol{\epsilon}}_{\boldsymbol{e}}^{\frac{(1-n)}{n}}. \tag{4}$$

In this equation E is the enhancement factor, B is a viscosity parameter that depends on ice temperature relative to the pressure melting point computed through an Arrhenius law, n is Glens flow law parameter (n=3), and the effective strain rate is defined as $\dot{\epsilon_e}^2 = tr(\dot{\boldsymbol{\epsilon}}^{\boldsymbol{2}})/2$. In all our simulations E is set to 1 which means that ice is modelled as an isotropic material.

2.2. Ice temperature

The ice temperature is determined through the heat transfer equation (e.g. Gagliardini et al., 2013) which reads

$$\rho c_v \left(\frac{\partial T}{\partial t} + \boldsymbol{u} \cdot T \right) = div(\kappa grad T) + \boldsymbol{D} : \boldsymbol{\sigma}, \tag{5}$$

where c_v and κ are the specific heat of ice and the heat conductivity, respectively. The **:** operator represents the colon product between two tensors. This last term of the equation represents strain heating.

2.3. Boundary conditions

2.3.1. Ice temperature

Our parameterisation of surface temperature changes follows Ritz et al. (2001). We parameterise relative surface temperature changes to present-day as a function of relative surface elevation change with respect to present-day elevations and a spatially uniform surface temperature variation that is derived from the nearby EDML ice core. The surface

temperature is then given by (Ritz et al. (2001), eq. 11):

$$T_a = T_{a0} - 0.00914(z_{s0} - z_s) + \Delta T_{clim}. \tag{6}$$

Here T_a and T_{a0} are the surface temperatures at the current timestep and present-day (from Comiso (2000)), z_s and z_{s0} are the surface elevations at the current timestep and present-day, and ΔT_{clim} is the climatic forcing derived from the EDML ice core. As in Ritz et al. (2001), we apply a spatially constant lapse rate of 0.00914°C/m (Table S1).

At the grounded underside of the ice sheet, where the ice in contact with the subglacial topography, we prescribe the geothermal heat flux (Martos et al., 2017). This heat flux is time invariant. Ice temperature is set to the local pressure melting point for the boundary condition underneath the floating ice shelves.

2.3.2. Surface mass balance (SMB) and basal mass balance (BMB)

A kinematic boundary condition determines the evolution of upper and lower surfaces z_j:

$$\frac{\partial z_j}{\partial t} + u_x \frac{\partial z_j}{\partial x} + u_y \frac{\partial z_j}{\partial y} = u_z + \dot{a}_j, \tag{7}$$

where $\dot{a}_j$ is the accumulation/ablation term and $j = (b, s)$, with s being the upper surface and b being the lower surface (base) of the ice sheet.

For the surface mass balance (SMB) parameterisation, we closely follow Ritz et al. (2001) again. However, we assume that no melt occurs in all our simulations. As for the surface temperature, our SMB parameterisation uses a present-day distribution of the SMB (Lenaerts et al., 2014) as input. Variations of the SMB over time are then proportional to the exponential of the surface temperature variation (Ritz et al. (2001), eq. 12):

$$\dot{a}_s(T_a) = \dot{a}_{s0}(T_{a0}) exp(\Delta a \cdot (T_a - T_{a0})), \tag{8}$$

where a_{s0} is the present-day SMB, a_s is the SMB at the current timestep, and the parameter $\Delta a = 0.07°C^{-1}$. This means that for a surface temperature drop of 10°C, the SMB is reduced by 50% (Ritz et al., 2001).

Sub-shelf melting underneath the floating ice shelves is based on the difference between the local freezing point of water under the ice shelves and the ocean temperature near the continental shelf break (Beckmann & Goosse, 2003). The freezing temperature (T_f) is calculated through:

$$T_f = 0.0939 - 0.057 S_o + 7.64 \times 10^{-4} z_b, \tag{9}$$

where S_o is the ocean salinity (Table S1). The basal melt rates ($\dot{a}_b$) are then computed by

$$\dot{a}_b = \frac{\rho_w c_{p_o} \gamma_T F_{melt} (T_O - T_f)^2}{L \rho_i}. \tag{10}$$

In this equation, ρ_w is the density of water, c_{p_o} is the specific capacity of the ocean mixed layer, γ_T is the thermal exchange velocity, L is the latent heat capacity of ice, F_{melt} is a tuning parameter to match present day melt rates, and T_O is the ocean temperature (Table S1). The ocean temperature is initially set to -0.52°C (Beckmann & Goosse, 2003). Applied variations of the ocean temperature are a damped (∼40%) and delayed (∼3,000 years) version of the climatic forcing for surface temperature ΔT_{clim} (Bintanja et al., 2005).

2.3.3. Basal sliding and sea-level

Where the ice is in contact with the subglacial topography a linear Weertman-type sliding law of the form

$$\boldsymbol{\tau_b} = C |\boldsymbol{u_b}|^{m-1} \boldsymbol{u_b}, \tag{11}$$

is employed. Here $\boldsymbol{\tau_b}$ is the basal traction, m is the basal friction exponent which is set to 1 in all simulations, and C is the basal friction coefficient. For the present-day grounded ice sheet, C is inferred by solving an inverse problem (see section 2.4), and for the present-day ocean beds a uniform basal friction coefficient of 10^{-1} MPa m^{-1} yr and 10^{-5} MPa m^{-1} yr is prescribed for the soft (sediment-based) bed and hard (crystalline rock-based) bed simulations. Underneath the floating part of the domain basal traction is zero ($\boldsymbol{\tau_b} = 0$), but hydrostatic sea pressure is prescribed.

We initialise the present-day sea-level to zero and apply sea-level variations according to Lambeck et al. (2014).

2.4. Model initialisation

The model is initialised to the present-day geometry using the commonly applied snapshot initialisation in which the basal traction coefficient C is inferred by matching observed ice velocities with modelled ice velocities. The same optimisation parameters as in Schannwell et al. (2019) are used. Similar to Zhao et al. (2018), we employ a two-step initialisation scheme. In the first iteration, the optimisation problem is solved with an isothermal ice sheet with ice temperature set to -10°C. The resulting velocity field is then used to solve the steady-state temperature equation before the optimisation problem is solved again with the new temperature field. This type of temperature initialisation approach should provide similar results to a computationally expensive temperature spin-up over several glacial cycles (Rückamp et al., 2018), as long as the system is close to steady state. There is growing evidence that this is the case for the Ekström Ice Shelf catchment (e.g. Drews et al., 2013; Schannwell et al., 2019).

2.5. Mesh generation and refinement

We initially create a 2D isotropic mesh with a nominal mesh resolution of ∼6 km everywhere in the domain. To ensure that we simulate grounding-line dynamics at the required detail, we use the meshing software MMG (http://www.mmgtools.org/, last access: 2 October 2019) to locally refine the mesh down to ∼1 km in the region of present-day Ekström Ice Shelf (Figure S2) with areas away from the region of interest remaining at ∼6 km resolution. The mesh is then vertically extruded, consisting of 10 layers and held fixed in time.

2.6. ParStokes

Because of the non-Newtonian rheology of ice and the dependence of viscosity on ice velocity, the resulting Stokes equations are non-linear and have to be solved iteratively. In three dimensions the arising systems of linear equations become large (10^6-10^7 degrees of freedom) very quickly. Standard iterative methods (Krylov supspace methods) in conjunction with algebraic preconditioners (e.g. Incomplete LU (ILU) decomposition) do not converge for most real-word geometries in glaciology. High aspect ratios of the finite elements and spatial viscosity variations of several orders of magnitudes, strongly affect accuracy and stability of the numerical solution (Malinen et al., 2013). This means that most glaciology application with Elmer/Ice revert to using a direct method for solving the Stokes equations. While robust, direct solvers do not take advantage of the sparse structure of the matrix and require large amounts of memory. In three dimensions their memory requirements increase with the square of the number of unknowns. Therefore, we use a stable parallel iterative solver (ParStokes) in our simulations that is implemented

in Elmer/Ice, but has so far been rarely used. ParStokes is based on the idea of block preconditioning (Malinen et al., 2013) that improves the solvability of the underlying saddle-point problem (via clustering of eigenvalues) such that Krylov subspace methods now converge. This results in a much better scaling of the required computation time with increasing numbers of Computer Processing Units (CPUs, Figure S3). For our simulations, the ParStokes solver is about 71-84% faster than the "classic" Elmer/Ice setup that uses a direct solver (Figure S4). As our problem size with ∼570,000 degrees of freedom is of medium size, there might be even more speed-up potential for larger problems by using more CPUs.

3. Reduction of computation time with the ParStokes solver

Full-Stokes simulations in 3D have thus far been restricted to timescales that are shorter than 1,000 years due to their high computational demands (Seddik et al., 2012; Favier et al., 2014; Schannwell et al., 2019). Simpler model variants omit one or several stress gradients in the underlying ice-flow equations, with partially unknown consequences for, for example, grounding-line migration behavior. It is therefore required to extent the simulation times of full-Stokes models. The vast majority of the computation time is spent on solving the non-linear equations for ice velocity. Here, we compare simulations of Elmer/Ice using the classic velocity solver setup employing a parallelized direct solver to a so far unused stable parallel iterative solver setup. The total compute time for the iterative solver is 80% faster. In our case this means that the 40,000-year simulation now takes 23 days instead of 141 days for the hard-bed case, and 27 days instead of 94 days for the soft-bed case (Figure S4). The time differences between both scenarios are due

to the differing grounding-line migration pattern, which require additional computation time for the hard-bed case. This significant speed-up unlocks a new time dimension for the applicability of 3D full-Stokes ice-sheet models on the regional scale while keeping a high mesh resolution. Our modelling approach using the complete mechanical model for ice flow together with a freely evolving grounding line without parameterisations can now be combined with simplified ice-sheet models using ensemble simulations (Briggs et al., 2014; Pollard et al., 2016). This provides an important step in reducing uncertainties regarding internal ice dynamics, a key process to a better understanding of grounding-line dynamics and processes occurring at the underside of the ice sheet.

4. Comparison between direct Stokes solver (MUMPS) and ParStokes

To ensure that the "classic" solver setup using the direct Solver MUMPS and the new iterative solver ParStokes provide the similar results, we compare grounding-line positions over time for the hard bed and soft bed simulations in this section. We note however that we do not expect a perfect match between the two solver setups due to small differences in the finite element formulation (e.g. stabilization method).

For both simulations, there is very good agreement in terms of grounding-line position over time, with differences never exceeding 5% (Figure S5). Because the soft bed simulation exhibits smaller magnitude grounding-line motion over the simulation, agreement between the two solver setups is better, with differences well below 1% for almost the entire simulation length. In the hard bed simulation, where larger magnitudes of grounding-line motion are modelled, the ParStokes solver's grounding-line is not as far advanced as the MUMPS solver grounding-line (Figure S6). Moreover, at times of rapid grounding-line

motion, the response of the grounding-line in the ParStokes solver is delayed. This leads to certain differences in transient grounding-line positions (<5%). However, the situation improves for steady state grounding-line positions (<1.5% difference).

The larger variations in grounding-line position coupled with the more extreme geometrical changes in the case of different grounding-line positions in the hard bed simulation also result in larger differences in ice thickness. Locally these differences can be as large as ∼460 m (<25% of the ice thickness). These differences are pronounced in the periods of delayed grounding-line response, but reduce once a stable grounding-line position has been reached (Figure S6, S7).

5. Grounding-line flux calculation

To compute present-day ice flux across the grounding line, we extract ice thickness from Bedmap2 (Fretwell et al., 2013) and ice velocities from the MEaSURES product (Rignot et al., 2011) along the present-day grounding line (Bindschadler et al., 2011). We then define the threshold for slower moving catchments as ≤300m/yr and compute the ice flux (velocity · ice thickness) and the percentage area that belongs to the category of slower moving catchments. This shows that 90% of the present-day Antarctic grounding-line is occupied by slower moving catchments and they account for ∼30% of the total ice flux across the grounding line.

6. Effect of ocean bed properties on estimated erosion rate

Due to our modelling approach, we have reduced uncertainties regarding the magnitude of basal sliding. However, significant uncertainties remain for basal processes such as erosion which we demonstrate in this section.

Erosion rates are commonly linked to the magnitude of basal sliding to some power (e.g. Herman et al., 2015; Koppes et al., 2015). This means that differences in basal properties (e.g. basal friction) of ocean beds affect computed erosion rates. Differences in basin-averaged erosion rates using two recently proposed erosion laws (Herman et al., 2015; Koppes et al., 2015) alone can be significant (up to 0.021 mm/yr). However, while the uncertainties surrounding the selected erosion law are already large, the effect of differing ocean bed properties is even larger (Figure S8). Even though absolute differences appear small when averaged over the basin ($\leq$0.022 mm/yr), when these mean erosion rates (10^{-7}-10^{-5} mm/yr for hard bed and $4{\cdot}10^{-5}$-$8{\cdot}10^{-4}$ mm/yr for soft bed) are used to estimate erosion volumes over a glacial cycle the variations are significant. This is a consequence of each time step contributing to the increasing difference, so that the cumulative effect becomes even larger (two orders of magnitude for the two different ocean bed simulations, Figure S8c). Erosion volumes are between $9.65{\cdot}10^{3}$-$5.46{\cdot}10^{5}$ m^3 for the hard bed and $1.28{\cdot}10^{6}$-$2.11{\cdot}10^{7}$ m^3 for the soft bed over the full glacial cycle.

This simple calculation assumes that all sediment is instantly eroded and no sediment transport takes place. Absolute numbers might be different, but the magnitude of the effect of different ocean bed properties on basal sliding velocities and erosion volumes will not change. This underlines the importance of an improved understanding of how much of ice flow is caused by internal deformation or basal sliding.

References

Beckmann, A., & Goosse, H. (2003). A parameterization of ice shelf-ocean interaction for climate models. *Ocean modelling*, *5*(2), 157–170.

Bindschadler, R., Choi, H., Wichlacz, A., Bingham, R., Bohlander, J., Brunt, K., ... Young, N. (2011). Getting around Antarctica: new high-resolution mappings of the grounded and freely-floating boundaries of the Antarctic ice sheet created for the International Polar Year. *The Cryosphere*, *5*(3), 569–588. doi: 10.5194/tc-5-569-2011

Bintanja, R., van de Wal, R. S., & Oerlemans, J. (2005). Modelled atmospheric temperatures and global sea levels over the past million years. *Nature*, *437*(7055), 125–128. doi: 10.1038/nature03975

Briggs, R. D., Pollard, D., & Tarasov, L. (2014). A data-constrained large ensemble analysis of Antarctic evolution since the Eemian. *Quaternary Science Reviews*, *103*, 91–115. doi: 10.1016/j.quascirev.2014.09.003

Comiso, J. C. (2000). Variability and Trends in Antarctic Surface Temperatures from In Situ and Satellite Infrared Measurements. *Journal of Climate*, *13*(10), 1674–1696. doi: 10.1175/1520-0442(2000)013⟨1674:VATIAS⟩2.0.CO;2

Drews, R., Martín, C., Steinhage, D., & Eisen, O. (2013). Characterizing the glaciological conditions at Halvfarryggen ice dome, Dronning Maud Land, Antarctica. *Journal of Glaciology*, *59*(213), 9–20. doi: 10.3189/2013JoG12J134

Favier, L., Durand, G., Cornford, S. L., Gudmundsson, G. H., Gagliardini, O., Gillet-Chaulet, F., ... Le Brocq, A. M. (2014). Retreat of Pine Island Glacier controlled by marine ice-sheet instability. *Nature Climate Change*, *4*, 117.

Fretwell, P., Pritchard, H. D., Vaughan, D. G., Bamber, J. L., Barrand, N. E., Bell, R., ... Zirizzotti, A. (2013). Bedmap2: improved ice bed, surface and thickness datasets for Antarctica. *The Cryosphere*, *7*(1), 375–393. doi: 10.5194/tc-7-375-2013

Gagliardini, O., Zwinger, T., Gillet-Chaulet, F., Durand, G., Favier, L., de Fleurian, B., ... Thies, J. (2013). Capabilities and performance of Elmer/Ice, a new-generation ice sheet model. *Geosci. Model Dev.*, *6*(4), 1299–1318. doi: 10.5194/gmd-6-1299-2013

Herman, F., Beyssac, O., Brughelli, M., Lane, S. N., Leprince, S., Adatte, T., ... Cox, S. C. (2015). Erosion by an Alpine glacier. *Science*, *350*(6257), 193–195.

Koppes, M., Hallet, B., Rignot, E., Mouginot, J., Wellner, J. S., & Boldt, K. (2015). Observed latitudinal variations in erosion as a function of glacier dynamics. *Nature*, *526*(7571), 100–103. doi: 10.1038/nature15385

Lambeck, K., Rouby, H., Purcell, A., Sun, Y., & Sambridge, M. (2014). Sea level and global ice volumes from the Last Glacial Maximum to the Holocene. *Proceedings of the National Academy of Sciences*, *111*(43), 15296–15303. doi: 10.1073/pnas.1411762111

Lenaerts, J. T., Brown, J., Van Den Broeke, M. R., Matsuoka, K., Drews, R., Callens, D., ... Van Lipzig, N. P. (2014). High variability of climate and surface mass balance induced by Antarctic ice rises. *Journal of Glaciology*, *60*(224), 1101–1110. doi: 10.3189/2014JoG14J040

Malinen, M., Ruokolainen, J., Råback, P., Thies, J., & Zwinger, T. (2013). Parallel Block Preconditioning by Using the Solver of Elmer. In P. Manninen & P. ster (Eds.), *Applied Parallel and Scientific Computing* (pp. 545–547). Berlin, Heidelberg: Springer Berlin Heidelberg.

Martos, Y. M., Cataln, M., Jordan, T. A., Golynsky, A., Golynsky, D., Eagles, G., & Vaughan, D. G. (2017). Heat Flux Distribution of Antarctica Unveiled. *Geophysical Research Letters*, *44*(22), 11,417–11,426. doi: 10.1002/2017GL075609

Pollard, D., Chang, W., Haran, M., Applegate, P., & DeConto, R. (2016). Large ensemble modeling of the last deglacial retreat of the West Antarctic Ice Sheet: comparison of simple and advanced statistical techniques. *Geosci. Model Dev.*, *9*(5), 1697–1723. doi: 10.5194/gmd-9-1697-2016

Rignot, E., Mouginot, J., & Scheuchl, B. (2011). Ice Flow of the Antarctic Ice Sheet. *Science*, *333*(6048), 1427–1430. doi: 10.1126/science.1208336

Ritz, C., Rommelaere, V., & Dumas, C. (2001). Modeling the evolution of Antarctic ice sheet over the last 420,000 years: Implications for altitude changes in the Vostok region. *Journal of Geophysical Research: Atmospheres*, *106*(D23), 31943–31964. doi: 10.1029/2001JD900232

Rückamp, M., Falk, U., Frieler, K., Lange, S., & Humbert, A. (2018). The effect of overshooting 1.5 °C global warming on the mass loss of the Greenland ice sheet. *Earth Syst. Dynam.*, *9*(4), 1169–1189. doi: 10.5194/esd-9-1169-2018

Schannwell, C., Drews, R., Ehlers, T. A., Eisen, O., Mayer, C., & Gillet-Chaulet, F. (2019). Kinematic response of ice-rise divides to changes in ocean and atmosphere forcing. *The Cryosphere*, *13*(10), 2673–2691. doi: 10.5194/tc-13-2673-2019

Seddik, H., Greve, R., Zwinger, T., Gillet-Chaulet, F., & Gagliardini, O. (2012). Simulations of the Greenland ice sheet 100 years into the future with the full Stokes model Elmer/Ice. *Journal of Glaciology*, *58*(209), 427–440. doi: 10.3189/2012JoG11J177

Zhao, C., Gladstone, R. M., Warner, R. C., King, M. A., Zwinger, T., & Morlighem, M. (2018). Basal friction of Fleming Glacier, Antarctica Part 1: Sensitivity of inversion to temperature and bedrock uncertainty. *The Cryosphere*, *12*(8), 2637–2652. doi:

10.5194/tc-12-2637-2018

Table S1. Numerical values of the parameters adopted for the simulations

Parameter	Symbol	Value	Unit
ice density	ρ_i	917	kg m^{-3}
ocean density	ρ_w	1028	kg m^{-3}
Glen's exponent	n	3	
Gravity	g	9.81	m s^{-2}
Enhancement factor	E	1	
Tuning parameter SMB	Δacc	0.07	C^{-1}
Ocean salinity	S_0	35.0	PSU
Heat capacity	c_{p_o}	3974	J kg^{-1} C^{-1}
Latent heat of fusion	L	3.35×10^{-4}	J kg^{-1}
Tuning parameter BMB	F_{melt}	0.383×10^{-4}	
Thermal exchange velocity	γ_T	1×10^{-5}	m s^{-1}

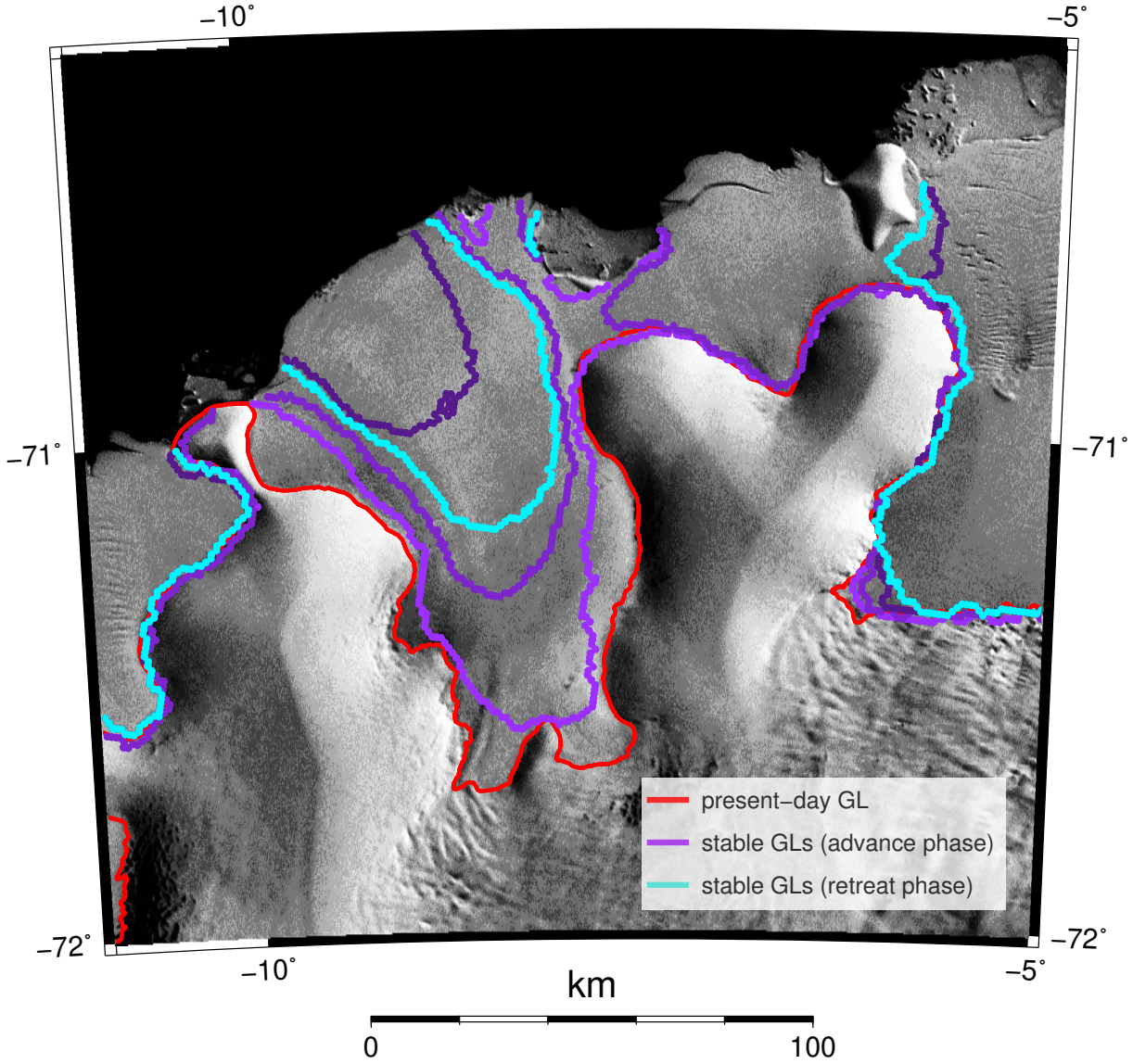

Figure S1. Modelled stable grounding-line positions from present-day back to the LGM (purple lines, advance phase) and from the LGM back to present day (cyan line, retreat phase).

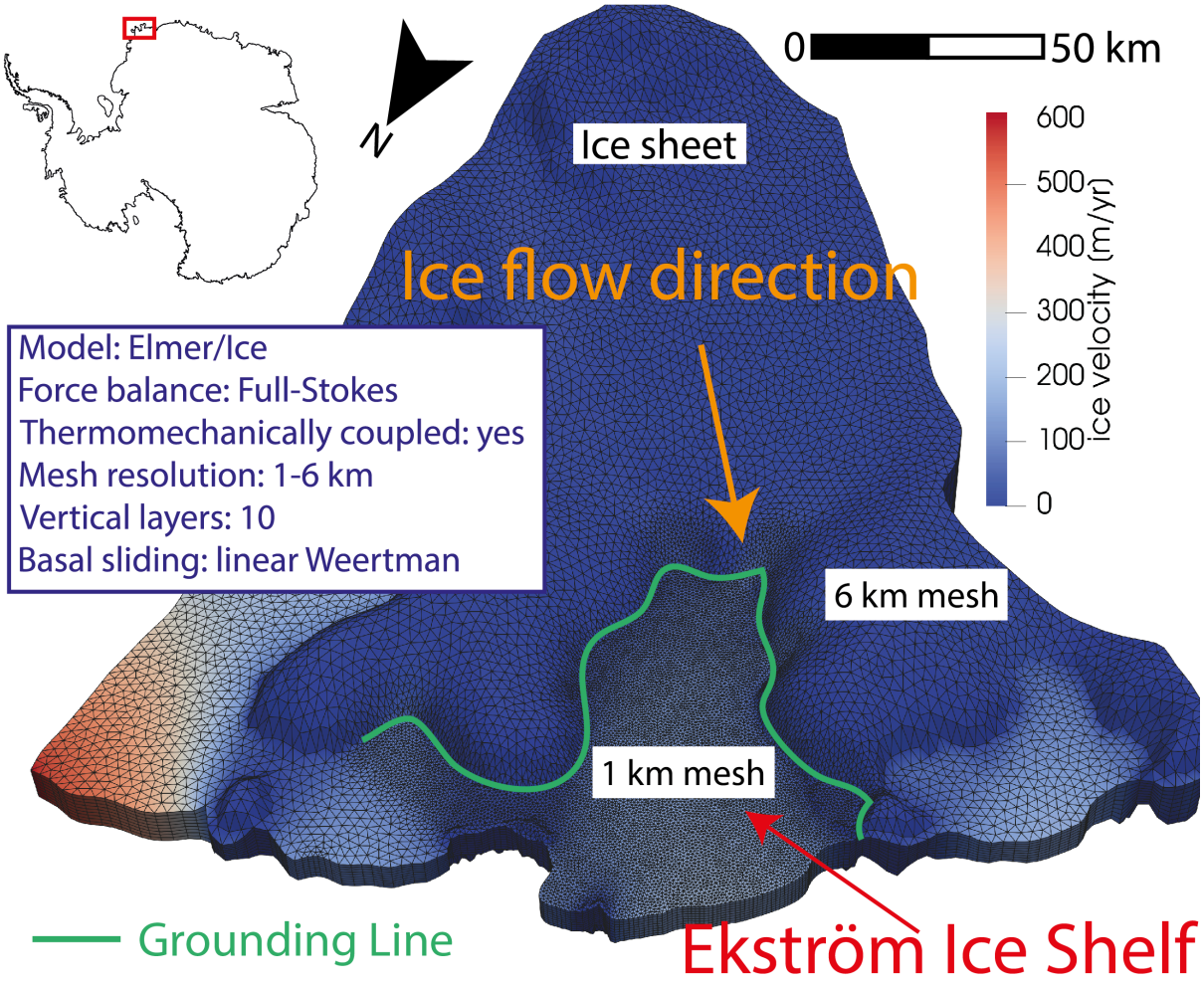

Figure S2. Model domain in 3D including numerical mesh of Ekström Ice Shelf catchment, East Antarctica

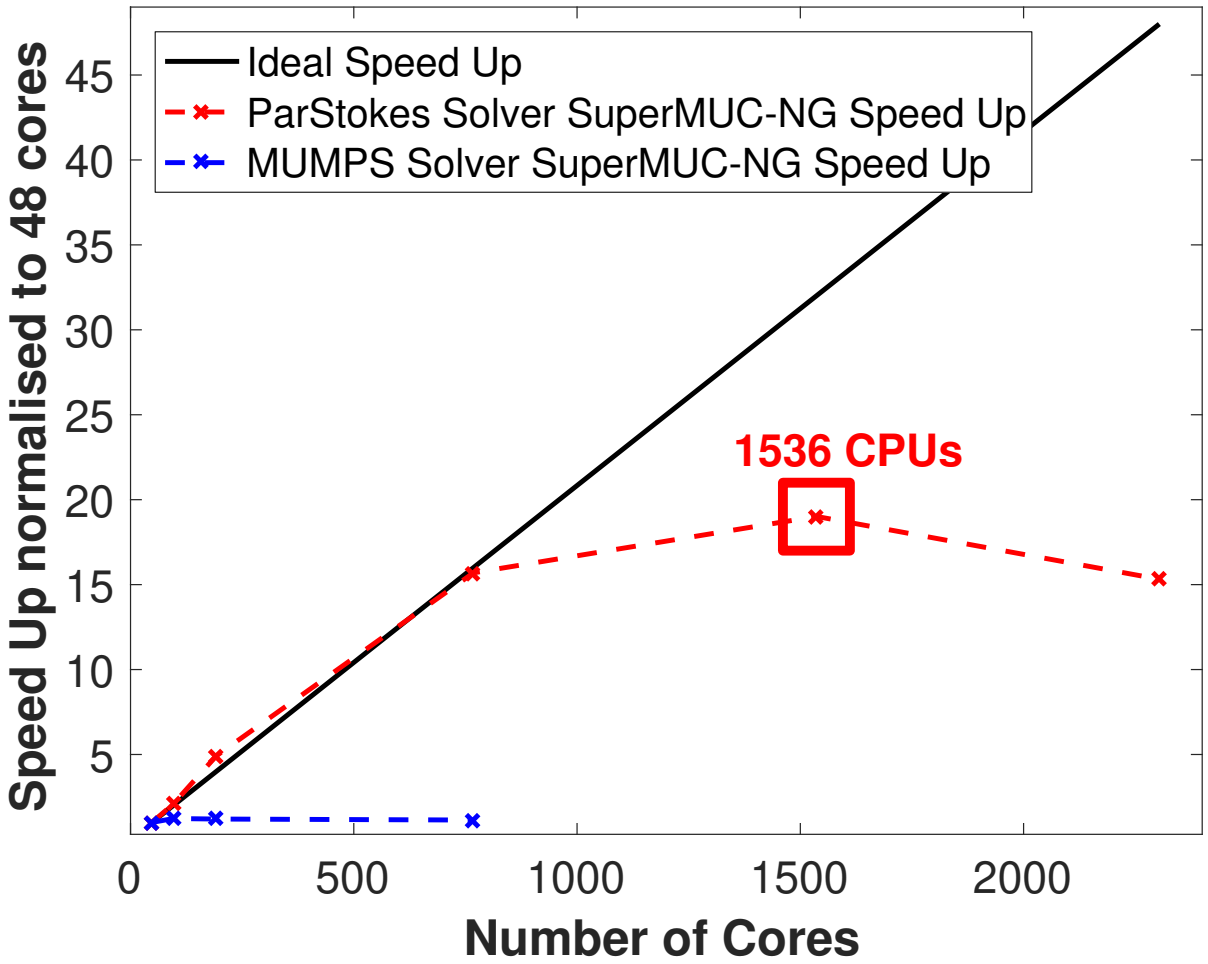

Figure S3. Scaling behaviour of iterative solver (ParStokes) and direct Solver (MUMPS) for Elmer/Ice on the SuperMUC-NG supercomputer in Munich.

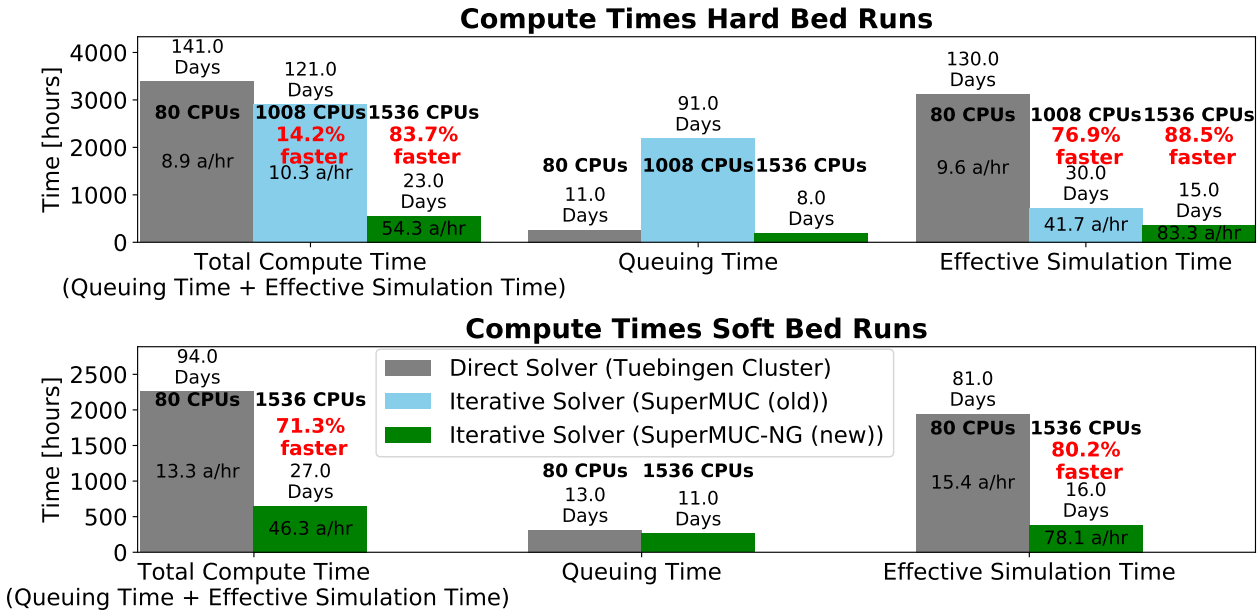

Figure S4. Speed-up of iterative Solver (ParStokes, green bars) in comparison to direct solver (MUMPS, gray bars) for the hard bed cavity (upper panel) and soft bed cavity (lower panel) simulations.

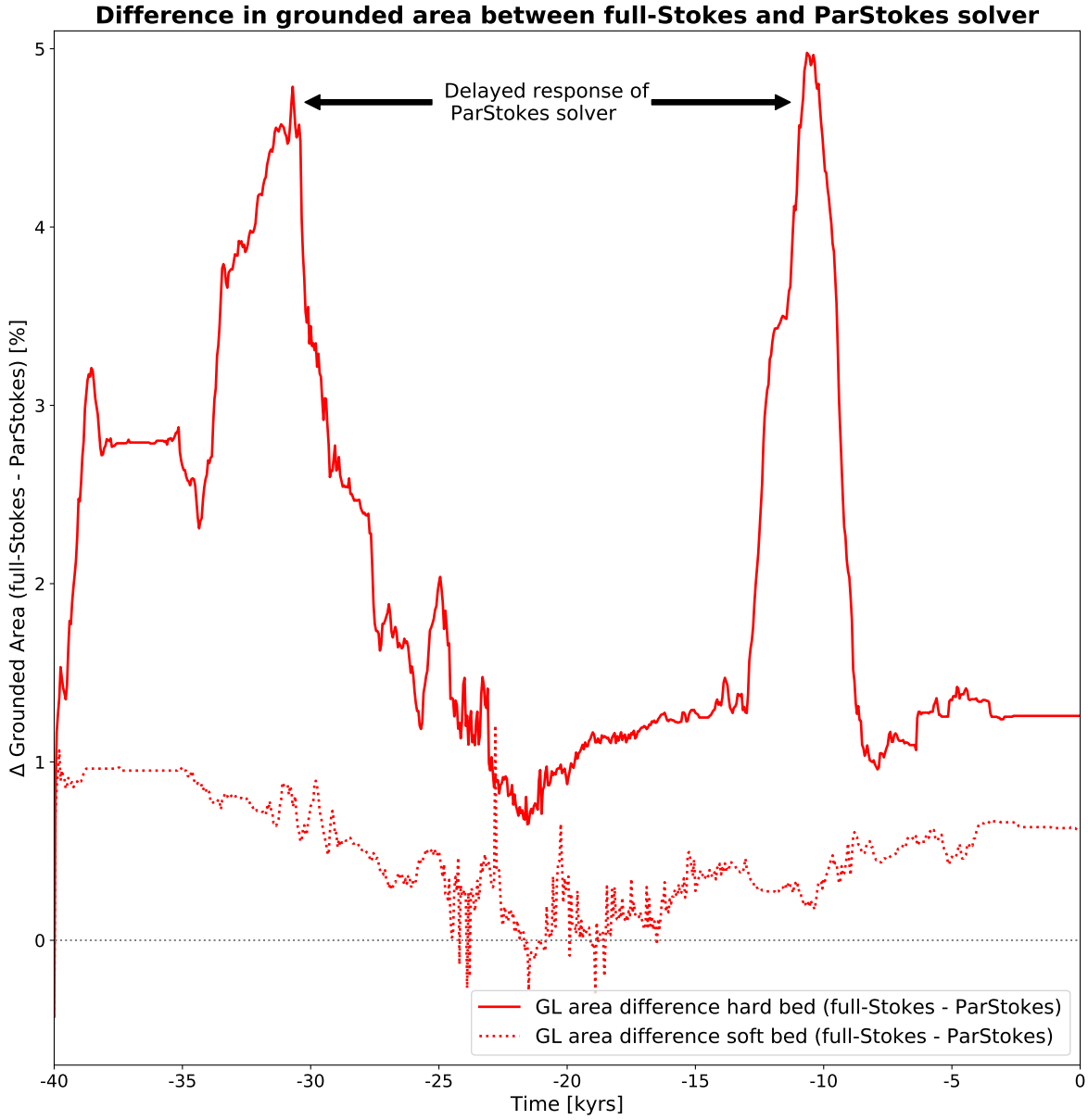

Figure S5. Differences in grounding-line (GL) area between the classic MUMPS and ParStokes solver setup for the soft bed and hard bed simulations.

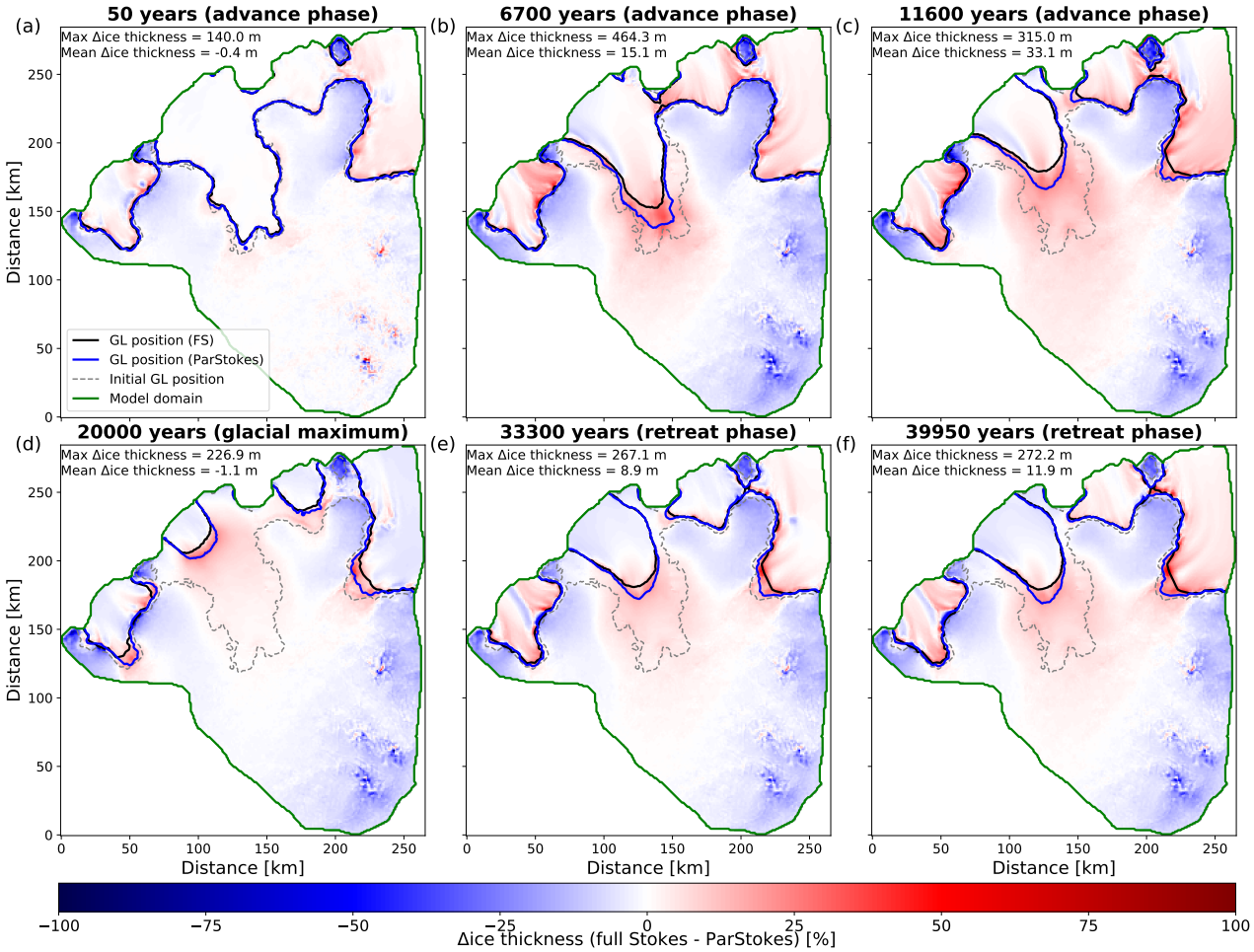

Figure S6. Differences in grounding-line position and ice thickness between the classic MUMPS and ParStokes solver setup for the hard bed simulation at specific time slices.

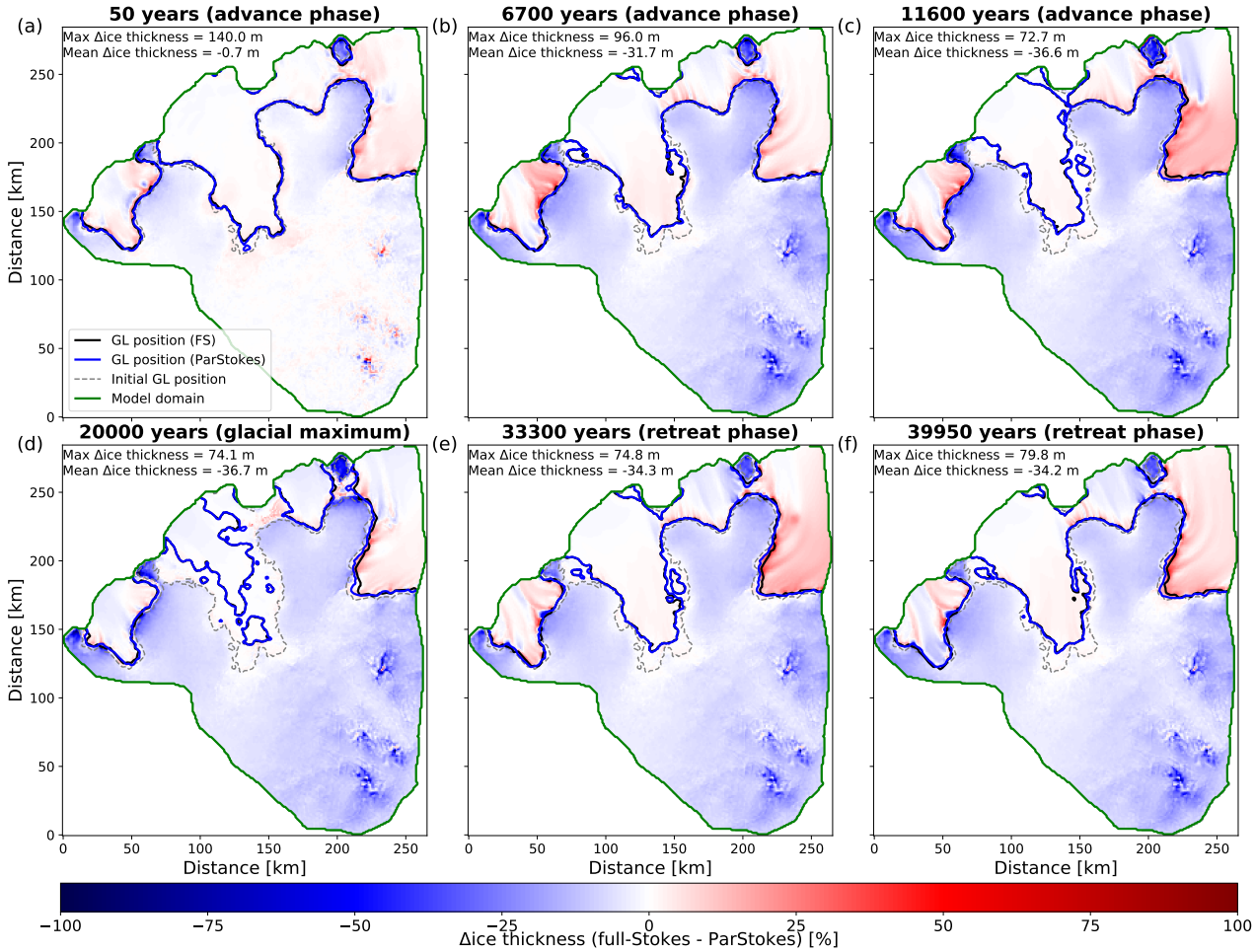

Figure S7. Differences in grounding-line position and ice thickness between the classic MUMPS and ParStokes solver setup for the soft bed simulation at specific time slices.

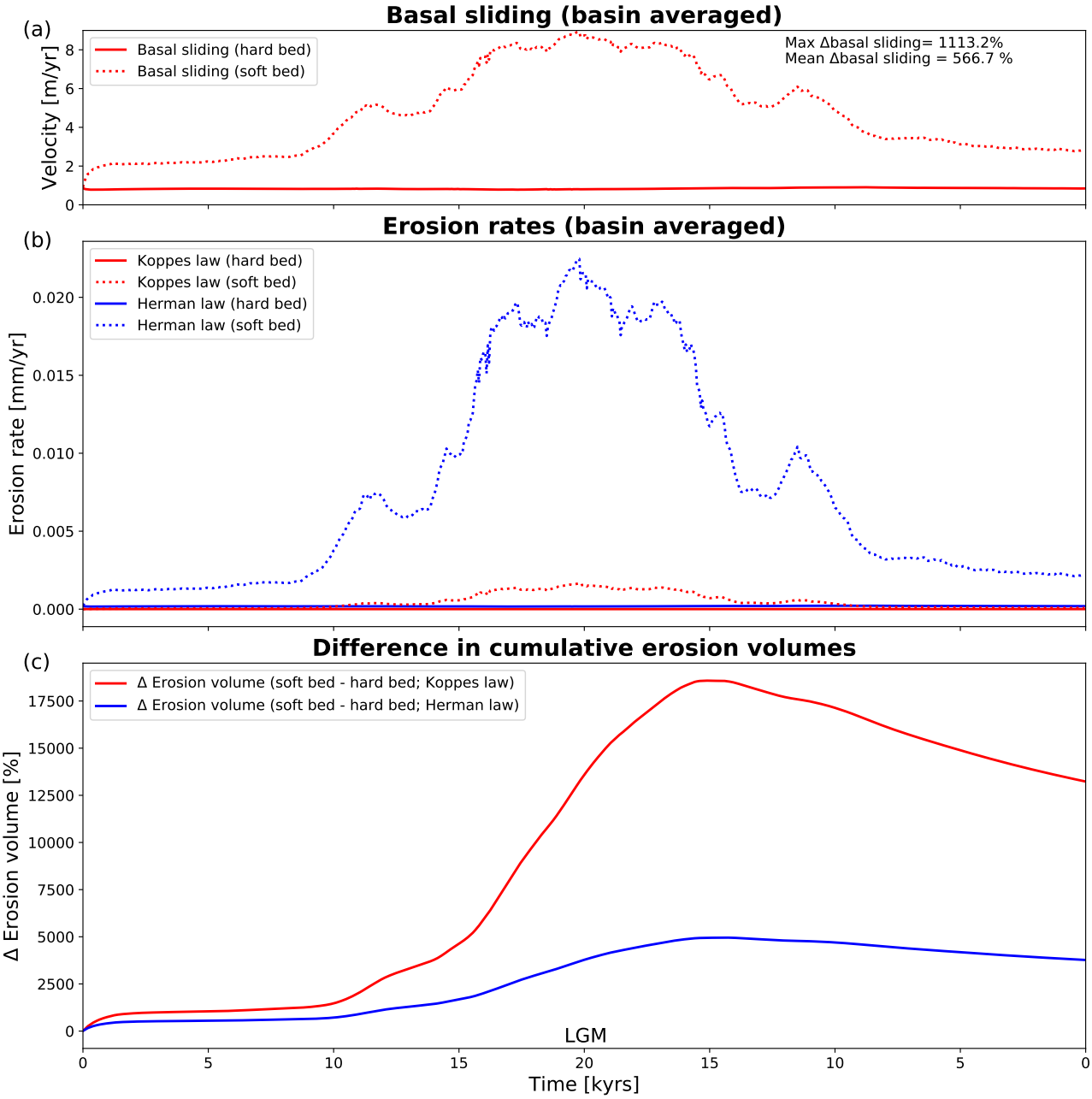

Figure S8. (a) basal sliding, (b) erosion rates, and (c) differences in cumulative erosion volumes for the hard bed and soft bed simulations using two different erosion laws.